Lab on a Chip

Cite this: *Lab Chip*, 2012, **12**, 1638

www.rsc.org/loc

PAPER

Single line particle focusing induced by viscoelasticity of the suspending liquid: theory, experiments and simulations to design a micropipe flow-focuser†

Gaetano D'Avino,[a] Giovanni Romeo,[a] Massimiliano M. Villone,[b] Francesco Greco,[c] Paolo A. Netti[ad] and Pier Luca Maffettone*[bd]

Received 23rd November 2011, Accepted 17th February 2012
DOI: 10.1039/c2lc21154h

We perform 3D numerical simulations, heuristic modeling and microfluidic experiments to demonstrate, for the first time, the presence of a bistability scenario for transversal migration of particles suspended in a viscoelastic liquid flowing in a pipe. Our results show that particle migration, either at the centerline or at the wall, can be controlled by the rheological properties of the suspending liquid and by the relative dimensions of the particle and tube. Proper selection of these parameters can promote strict aligning of particles on a line, *i.e.*, 3-D focusing. Simple design rules are given to rationally control particle focusing under flow in micropipes.

1 Introduction

In many systems, both natural and man-made, particles are transported in flowing fluids. Understanding particle dynamics in such heterogeneous systems is generally quite a difficult problem. Yet, the capability to control trajectories of suspended particles under continuous flow is in demand in a variety of analytical and processing issues, including separation, sorting, counting, and detection.[1] Cutting edge techniques are based on microfluidic cells carefully designed for specific particle-patterning aims.[2]

Patterning under flow usually requires particle migration, *i.e.*, motions somehow transversal to the main-stream direction. Such cross-flow movement can be non-invasively promoted by applying some external field (*e.g.*, electric or magnetic), however this requires specific properties of the particles.[3] Self-patterning, *i.e.*, patterning based on hydrodynamics only, can also be profitably obtained. For example, inertial forces have been cleverly exploited to drive migration in confined environments.[4–6] Efficient processes with this approach face several puzzling technical issues as complex flow cells are needed, while confinement and particle smallness tend to induce only weak inertial effects,[7] hence calling for rather large flow rates to achieve effective migration.

Another kind of fluid-dynamically driven patterning has been obtained, in the absence of inertia, by use of a rheologically complex suspending liquid.[8] In this case, a transversal driving force is established even in simple flow cells, because of the viscoelasticity of the flowing suspending medium. Indeed, focusing of microsized spheres on a plane, the so-called 2D focusing,[9] has been achieved in simple microslit flows. Such a viscoelastic focusing is promising, as the forces acting on the particles can be finely tuned by properly tailoring the suspending fluid rheology.

Of course, the ability to generate single-file particles (the so-called 3D-focusing[9]) is important in several applications. In flow cytometry, for example, single-line focusing of cells (achieved with an ingenious and complex flow assembly) allows a laser beam to efficiently interrogate them one at a time.[6,9]

Recently, a novel approach for 3D hydrodynamic sheathless focusing in straight channels has been proposed.[10] By properly balancing elastic and inertial forces (working in opposite directions), particle focusing along the channel centerline is achieved. To make elastic and inertial effects comparable, the flow rate needs to be carefully chosen. As a result, this so-called *Elasto-Inertial Focusing* works in a specific range of flow rates that depends on the geometrical parameters and fluid rheological properties. When applied to micrometric flows, relatively high flow rates are needed to turn on inertial effects. To our knowledge, this is the first technique allowing 3D focusing in straight channels based on hydrodynamic effects only. Recently, the Elasto-Inertial effect has also been successfully exploited for particle separation.[11]

In this paper, we demonstrate how focusing on a single line can be obtained through viscoelasticity-induced migration of non-colloidal spheres in pressure-driven flows in simple cylindrical

[a]*Center for Advanced Biomaterials for Health Care @CRIB, Istituto Italiano di Tecnologia, P.le Tecchio 80, 80125 Naples, Italy*
[b]*Department of Chemical Engineering, University of Naples Federico II, P.le Tecchio 80, 80125 Naples, Italy*
[c]*Istituto di Ricerche sulla Combustione, IRC-CNR, P.le Tecchio 80, 80125 Naples, Italy*
[d]*Interdisciplinary Research Center in Biomaterials (CRIB), University of Naples Federico II, P.le Tecchio 80, 80125 Naples, Italy. E-mail: pierluca.maffettone@unina.it; Fax: +39-081-2391800; Tel: +39-081-7682282*

† Electronic supplementary information (ESI) available. See DOI: 10.1039/c2lc21154h

micropipes in a wide range of flow rates, for dilute suspensions. The operating conditions are such that inertia is irrelevant, thus the focusing comes from purely elastic effects. Detailed 3D computation of the flow problem is used to guide the rheo-engineered design of microfluidic focusing units. Experiments are performed to show the practical feasibility of the alignment of microspheres in a microfluidic pipe, and to validate the simulation results. A simple heuristic argument is also given, which faithfully reproduces the simulation results. On the basis of the good quantitative agreement between experiments and simulations, the heuristic model gives simple rules for effectively designing a viscoelastic flow focuser.

2 Modeling

In this paper we analyze particle focusing from a dilute suspension of spheres. Diluteness allows us to proceed by considering the one body problem, *i.e.*, we consider a single rigid, non-Brownian, inertialess, spherical particle suspended in a viscoelastic fluid flowing in a cylindrical channel. The particle moves due to the imposed flow, and its rigid-body motion is completely defined by the translational velocity, denoted by $\boldsymbol{V}$, and the angular velocity, $\boldsymbol{\Omega}$. The particle translational velocity in cylindrical coordinates $r\theta z$ is then $\boldsymbol{V} = (V_M, 0, V_T)$, with V_M and V_T as the radial and axial components, respectively. The crossflow migration velocity, when it exists, is just V_M.

Assuming isothermal and inertialess flow, the governing equations for the fluid domain are:

$$\nabla \cdot v = 0 \tag{1}$$

$$\nabla \cdot \sigma = \mathbf{0} \tag{2}$$

$$\sigma = -pI + \tau \tag{3}$$

which are the equations for the mass balance, the momentum balance, and for the total stress. In these equations $\boldsymbol{v}$ is the velocity, σ the total stress tensor, p the pressure and $\boldsymbol{I}$ the unit tensor. The non-Newtonian stress tensor $\boldsymbol{\tau}$ needs to be specified by choosing a constitutive equation. In this work, we will consider the Giesekus constitutive model:[12]

$$\lambda \overset{\nabla}{\boldsymbol{\tau}} + \frac{\alpha\lambda}{\eta_0}\,\boldsymbol{\tau}\cdot\boldsymbol{\tau} + \boldsymbol{\tau} = 2\,\eta_0 \boldsymbol{D} \tag{4}$$

where the symbol ($^{\nabla}$) denotes the upper-convected time derivative,[12] $\boldsymbol{D} = (\nabla \boldsymbol{v} + (\nabla \boldsymbol{v})^T)/2$ is the rate-of-deformation tensor, and η_0 the zero-shear viscosity.

The constitutive eqn (4) is prototypical, and has indeed been used to describe a wide class of liquids encompassing polymer solutions and melts, biological and food fluids. The Giesekus liquid (as any viscoelastic liquid) brings to the hydrodynamics a characteristic time scale λ, measuring the fluid memory;[13] stress buildup or relaxation in the liquid takes place on this time scale, and the Newtonian limit corresponds to $\lambda = 0$. The inner time λ has to be compared with the external time, *i.e.*, the characteristic time scale t_f of the imposed flow; we take $t_f = 2\pi R^3/Q$ for the pipe flow, with Q being the flow rate. So, quite naturally, a dimensionless parameter arises, the so-called Deborah number $De = \lambda/t_f$; the Newtonian limit corresponds to $De = 0$, since the Newtonian liquid has no inner time, whereas, by increasing De, nonlinear viscoelastic effects become substantial. Notice that, in this context, the Deborah number is equivalent to the Weissenberg number used in previous works.[10,11]

Under steady state simple shear flow, and at very low shear rates, the Giesekus model predicts a constant viscosity, and first and second normal stress differences N_1 and N_2, *i.e.*, elastic stresses,[12] quadratic in the shear rate $\dot{\gamma}$. By increasing the shear rate, the viscosity and both normal stress coefficients ($\Psi_1 = N_1/\dot{\gamma}^2$and $\Psi_2 = N_2/\dot{\gamma}^2$) all decrease with the shear rate, *i.e.*, they are *shear thinning*. In the Giesekus model, the parameter α modulates the extent of the thinning. A limiting case is $\alpha = 0$, corresponding to constant viscosity and normal stress coefficients, hence recovering the well-known Oldroyd-B model.[12]

No-slip conditions are assumed on the channel walls, and periodicity is prescribed between the inflow and outflow sections, together with a flow rate Q in inflow. The boundary condition on the particle surface is the no-slip condition *plus* the rigid-body motion:

$$\boldsymbol{u} = \boldsymbol{V} + \boldsymbol{\Omega} \times (\boldsymbol{r}_s - \boldsymbol{r}) \tag{5}$$

where $\boldsymbol{r}$ is the position of the particle center, and $\boldsymbol{r}_s$ describes a point on the spherical surface S. In eqn (5), both the translational and the angular velocities of the sphere are unknown. They are obtained from the condition that the external forces and torques on the particle are nil,[14] because of the no-inertia assumption. The particle position is updated by integrating the kinematic equation:

$$\frac{d\boldsymbol{r}}{dt} = \boldsymbol{V}, \boldsymbol{r}|_{t=0} = \boldsymbol{r}_0 \tag{6}$$

which gives the trajectory of the particle.

The governing equations are solved by the finite element method. Tetrahedral elements have been chosen to discretize the computational domain. To stabilize the numerical code at (moderately) high Deborah numbers, a DEVSS-G formulation is adopted[15,16] combined with the SUPG technique[17] and a log-conformation representation for the conformation tensor.[18,19] The particle motion is taken into account by using an ALE formulation (Arbitrary Lagrangian–Eulerian),[20] whereby at each time step the mesh nodes follow the particle motion and are moved according to a mesh velocity obtained by solving an extra equation. A detailed description of the numerical method, the corresponding weak formulation and the time-stepping procedure can be found elsewhere.[14,21]

3 Simulation results - what we learn from the model

Three nondimensional parameters have to be chosen to specify the geometry and the rheology of the system; they are the so called blockage ratio $\beta = a/R$ (the particle and the channel radii are denoted by a and R, respectively), the purely constitutive parameter α, and the dimensionless measure of the flow intensity De. Fig. 1 shows the computed trajectories of particles starting at different initial radial positions r_0 in the pipe, for $\beta = 0.1$, $\alpha = 0.2$, and $De = 2.0$. These values were selected as representative of a situation where the geometry allows for wall effects on particle motion without severely constraining the particle, and the

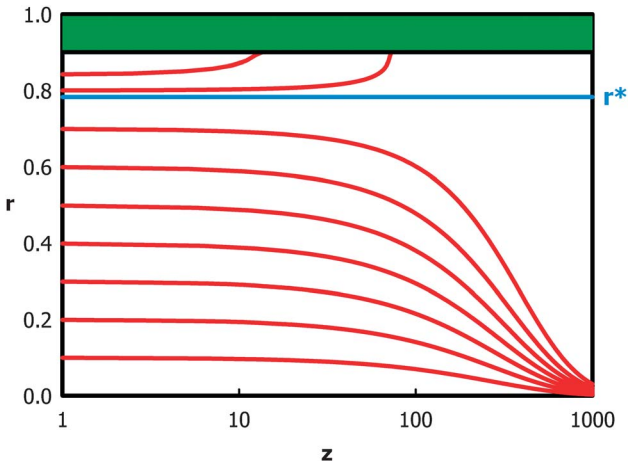

Fig. 1 Trajectories of the radial position of the sphere calculated for $De = 2$, and $\beta = 0.1$, for different initial positions. The fluid is a shear thinning Giesekus liquid with $\alpha = 0.2$. The particle position r and its axial position z are made dimensionless with R. The cyan line $r = r^*$ is the neutral cylindrical surface (see text). The green area is the unaccessible channel region due to the finite particle size and the excluded volume effect.

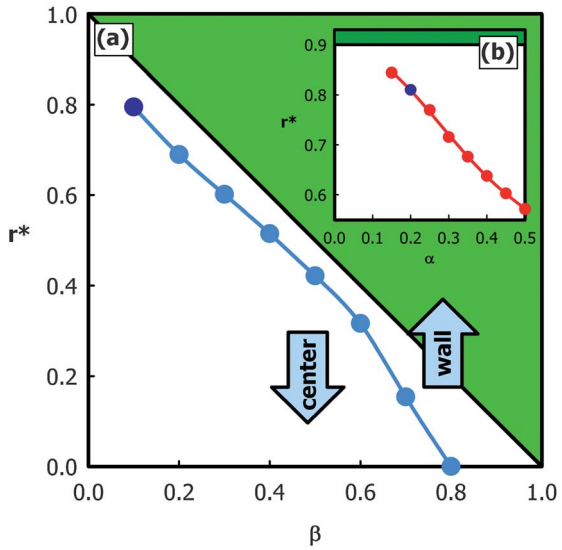

Fig. 2 (a) Computed radial position r^* of the neutral surface as a function of the blockage ratio β for the Giesekus fluid with $\alpha = 0.2$, at $De = 2$. Particles starting above r^* migrate towards the wall, while those below go to the centerline. Notice that, for computational limitations, data below $\beta = 0.1$ could not be calculated. (b) Computed radial position r^* of the neutral surface as a function of the parameter α for the Giesekus fluid, with $\beta = 0.1$ at $De = 2$. The position of the neutral surface moves towards the wall as the shear-thinning decreases, thus enlarging the centerline-attractive region. The dark blue circle in both figures corresponds to the parameters: $\beta = 0.1$, $\alpha = 0.2$, $De = 2$. The green area is the unaccessible channel region due to the finite particle size and the excluded volume effect.

viscoelastic properties of the suspending liquid are well active. Cross-flow migration is apparent in the figure, and results from purely viscoelastic effects, as no migration at all would be observed in a Newtonian suspending liquid, in the absence of inertia.

Migration occurs in opposite directions depending on the initial radial position of the particle: sufficiently close to the pipe wall, migration is towards the wall, otherwise migration is towards the pipe centerline. A neutral cylindrical surface $r = r^*$ is then found, from which outward motions originate. Hence, an instability scenario characterizes the dynamics close to $r = r^*$; when the particle center is at r^*, no transverse motion occurs, but any disturbance in the radial direction triggers the migration. This phenomenology represents the inversion of the well-known Segré–Silberberg effect[22] for migration of particles in pipe flow of Newtonian liquids, *at finite inertia*. Indeed, the attracting cylindrical surface they found becomes a repelling one here, and their inertia-driven migration is substituted by a viscoelasticity-driven migration.

The main result obtained here is the alignment on a 1-D line, *i.e.*, the focusing of particles at the pipe centerline (3D-focusing), which is achieved merely through the viscoelastic features of the suspending liquid. It should be emphasized that a substantial focusing is gained at $z/R \gg 1$ (for example, from Fig. 1, it is $z/R \cong 10^3$), which opens the way to realistic applications with noncolloidal particles in microfluidics.

The position of the neutral surface $r = r^*$ depends on the three dimensionless parameters of the problem. In order to maximize the attraction of the centerline, we must understand how those parameters influence r^*. Still for the simple pipe flow, some simulation results of systematic campaigns of variation of the parameters are shown in Fig. 2, where the radial position of the neutral surface $r = r^*$ is plotted *versus* the blockage ratio β, at $De = 2$ and $\alpha = 0.2$. It is apparent that the quantity of particles eventually reaching the pipe center or the wall can be tuned by changing β. The effect of α (at a fixed β) is shown in the inset. It is found that small βs and αs promote focusing at the pipe centerline.

In physical terms, the effect of α means that pronounced shear-thinning increases the wall attraction. At the other extreme, *i.e.*, in the limiting case of $\alpha = 0$ (Oldroyd-B model), an inward migration is predicted, regardless of the particle initial position. Finally, concerning the influence of the Deborah number (not shown in the figure), we find that higher De values promote wall attraction.

In the next two sections, the main findings illustrated above will be validated through experiments.

4 Experiments

4.1 Materials and apparatus

To investigate the effects of the fluid rheology on particle migration, two viscoelastic fluids are prepared. The first fluid is an aqueous solution of 8% wt polyvinylpyrolidone (PVP, $M_w =$ 360 KDa, from Sigma-Aldrich). The second fluid is a 1% water solution of PEO ($M_w = 4000$ KDa, from Sigma-Aldrich). The two fluids were selected in view of their substantial viscoelasticity, and of their different shear thinning behavior.

The rheological properties of the fluids are measured in a rotational rheometer (ARG2, TA Instruments), with plate-plate and cone-plate geometries and with diameters of 40 mm. Fig. 3a and Fig. 3c show the dependence of the steady state

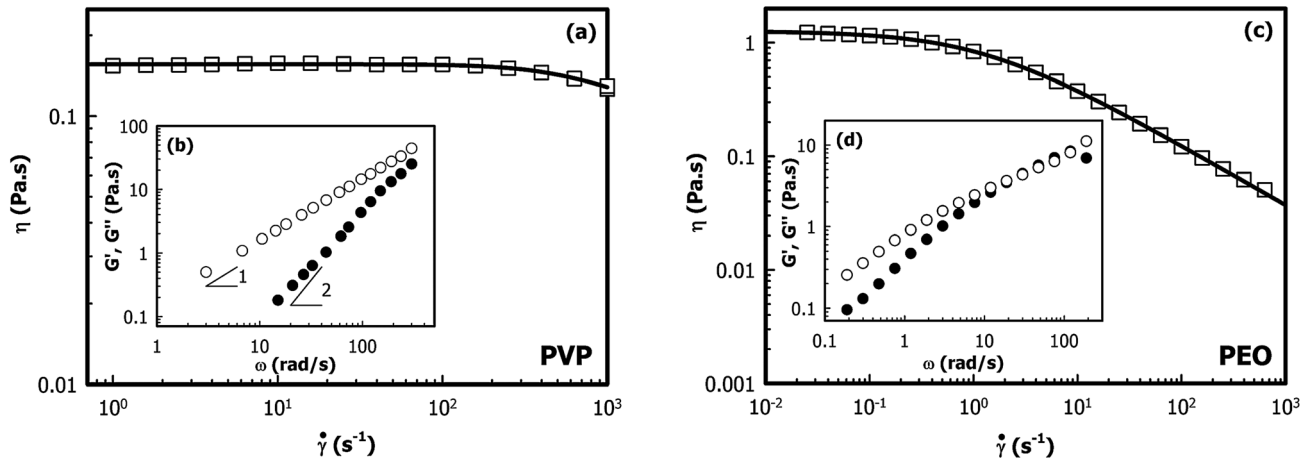

Fig. 3 (a) Measured steady shear viscosity η (white squares) for the aqueous 8% wt PVP solution. The solid line is a guide for the eye. (b) Measured elastic modulus G' (black circles) and loss modulus G'' (white circles) for the aqueous 8% wt PVP solution. The slopes indicate the frequency dependence expected in the terminal region for a viscoelastic fluid. (c) Measured steady shear viscosity η (white squares) for the PEO solution. The solid line is a guide for the eye. (d) Measured elastic modulus G' (black circles) and loss modulus G'' (white circles) for the PEO solution.

viscosity on the shear rate. In the case of PVP, the viscosity remains essentially constant over three decades of shear rate, with the appearance of a very weak shear-thinning effect at the highest shear rates. Linear viscoelasticity measurements in Fig. 3b show the frequency dependence of the viscoelastic moduli G' and G'' of PVP solution. Both moduli display the terminal behavior of a viscoelastic liquid, with $G' \propto \omega^2$ and $G'' \propto \omega$. The data require a spectrum of relaxation times to be adequately fitted. This implies that we should consider a multi-mode version of the constitutive equation. To simplify the computations, we estimate the characteristic relaxation time by the cross of the moduli trends. The estimate gives λ in the range of 2×10^{-3} s $\leq \lambda \leq 3 \times 10^{-3}$ s, which is in good agreement with the value $\lambda = 2.3 \times 10^{-3}$ s obtained by Yang *et al.*[10] with Caber measurements. The rheological characterization shows that the PVP solution is a good realization of an Oldroyd-B fluid, *i.e.*, a Giesekus liquid with $\alpha = 0$ that shows a constant viscosity.

We remark that the measured viscosity is constant up to a shear rate of about 200–300 s^{-1}. We calculated the maximum shear rate (at the wall) achieved in the channel for the highest flow rate considered in the experiments by solving the flow in a tube for a fluid with the same viscosity trend of the PVP. We found that the maximum shear rate is around 150 s^{-1} that allows us to consider a viscosity-constant model.

The steady state viscosity of PEO solution in Fig. 3c shows a Newtonian plateau followed by a pronounced shear-thinning behaviour at large shear rates. The power law dependence of the shear thinning region is around -0.5. The frequency dependence of the viscoelastic moduli G' and G'' reported in Fig. 3d displays a strong elastic component, though the terminal region is not visible in the investigated frequency range. The intersection of the linear moduli roughly gives a characteristic relaxation time around $\lambda \cong 4 \times 10^{-2}$ s. The PEO solution can be assimilated to a Giesekus fluid with a non-zero α.

On the basis of the simulations, we have designed simple focusing microfluidic apparatus for particles of a few microns diameter. As focusing implies that the vast majority of particles should migrate towards the channel centerline, a relatively low blockage ratio and a suspending liquid with a low degree of shear-thinning should be preferred, in order to achieve alignment within a reasonable length of the micro-pipe (a few centimeters, say). The PVP solution is then selected as the suspending liquid because of its very weak shear-thinning effect. On the other hand, the strongly shear thinning PEO solution will be used to highlight the bistability scenario.

Flow focusing experiments are carried out in a glass cylindrical capillary (inner radius $R = 25$ μm, outer diameter of 80 μm, length $L = 10$ cm, from Vitrocom). The capillary is glued to one end of a feeding silicon microtube with an inner radius of 125 μm and a length of about 30 cm. The other end of the silicon tube is immersed in a vial containing the polystyrene (PS) particles suspended in the viscoelastic fluid at a volume fraction $\phi \simeq 0.1\%$. Before each experiment the suspension is stirred for one hour and sonicated for about three minutes. The particles are synthesized using a standard seed emulsion polymerization technique[23] allowing us to obtain monodisperse spherical particles with an average diameter $2a$ of about 4 μm, as measured from microscopy. The polystyrene particles have a density of 1.05 g ml^{-1}, whereas we can safely assume that the PVP as well as PEO–water solutions have a density of 1 g ml^{-1}. A simple estimation of the sedimentation velocity from the Stokes law shows that for our particle size and liquid zero-shear viscosity, this density mismatch cannot induce any relevant particle displacement in our experimental timescales.

The vial containing the suspension is closed in a pressure controlled pump (Mitos P-Pump, Dolomite Microfluidics). This system allows variation of the pressure drop Δp in the capillary from 0.001 to 10 bar.

Particles flowing in the capillary are observed through a microscope (Reichert–Jung) with an overall magnification of 125×. Image sequences of the flowing solution are collected with a fast camera (IGV-B0620M, Imperx) at a frame rate of 260 fps. All the experiments are performed at room temperature ($T = 21$ °C ± 1).

4.2 Experimental results - theory validation

The centerline attraction is demonstrated by use of the PVP solution. We vary the applied pressure drop Δp from 0.1 to 6 bar, corresponding to measured flow rates Q ranging from about 0.0075 to 0.75 μl min^{-1}. These flow rates give a Deborah number varying from 0.004 to 0.4. Notice that, at the highest flow rate, we estimate a Reynolds number of order of magnitude 10^{-3}, assuring that inertial effects are in fact irrelevant. For $\Delta p < 2$ bar, we do not observe particle alignment within the length of the channel. The situation changes as Δp is increased. For $\Delta p = 2$ bar, corresponding to $Q \cong 0.15$ μl min^{-1} and $De \cong 0.06$, we find that the particle radial distribution strongly depends on the distance from the inlet L_z. This is shown in Fig. 4 where we report snapshots of particle positions at three different distances from the inlet (the corresponding movies are available as Supplementary Material†). At 2.5 cm from the inlet ($L_z/R = 10^4$) we find that the particles are still randomly distributed along the radial direction, as shown in Fig. 4a. However, at 3.5 cm from the inlet ($L_z/R = 1.4 \times 10^4$), the particles are already confined within a narrow band around the channel centerline, as reported in Fig. 4b. Finally, at 4.5 cm from the inlet ($L_z/R = 1.8 \times 10^4$), we observe strict particle focusing along the central streamline, see Fig. 4c.

To validate the numerical predictions, we compare the experimental particle radial distributions with the simulated ones obtained in the same conditions. The experimental radial distributions of the particles are calculated starting from the velocities of the particles along the flow direction. After measuring the horizontal particle velocities V_T and assuming a parabolic flow profile within the channel cross-section (an assumption justified by the constancy of the viscosity of the PVP solution), we calculate the particle radial position r as:

$$r = R\sqrt{1 - \frac{V_T(r)}{V_{T,max}}} \tag{7}$$

where $V_{T,max}$ is the velocity of a particle flowing in the center of the channel. We measure $V_{T,max}$ from the velocities of the particles far away from the inlet, *i.e.* $L_z \geq 5$ cm. Indeed, as shown in Fig. 4, at those distances all the particles move along the channel centerline. Notice that, in writing eqn (7), we assume that the particle moves at the same local velocity as the fluid. For the blockage ratio considered here, this approximation introduces an error lower than 0.5%.[24]

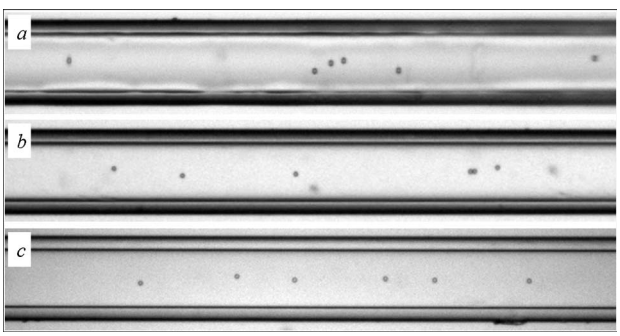

Fig. 4 Experimental particle distribution in a straight cylindrical micropipe at different distances from the inlet with water solution at 8% PVP. The applied pressure drop is $\Delta p = 2$ bar, corresponding to a flow rate $Q = 0.15$ μl min^{-1} and a Deborah number $De \cong 0.06$. At 2.5 cm from the inlet (a) no alignment is observed and the particles are still randomly distributed. At a distance of 3.5 cm from the inlet (b) the particles are confined within a narrow band around the centerline. At 4.5 cm from the inlet (c) 3D focusing on a line is achieved.

To calculate the fraction of particles in a certain band at a distance r from the center, we subdivide the cross-section of the tube in an inner circle of radius $r = 2a$ (denoted by an index $k = 1$) and in concentric annular rings with thickness $\Delta r = 2a$ (denoted progressively by indices $k = 2,3,\ldots$ moving from the center towards the channel wall). The normalized fraction $f_k(L_z)$ of particles in the radial band k is then calculated as:

$$f_k(L_z) = \frac{\dfrac{n_k(L_z)}{A_k \bar{v}_k}}{\sum_k \dfrac{n_k(L_z)}{A_k \bar{v}_k}} \tag{8}$$

where $n_k(L_z)$ is the number of particles flowing in the band k at a fixed distance L_z from the inlet, and A_k and $\bar{v}_k$ are the cross-sectional area and the average velocity of the band k, respectively. Such a definition is dictated by the fact that: i) along the radial direction, bands with the same thickness Δr have different areas A_k, meaning that a higher number of particles is expected for bands at larger radial distances, ii) the average velocity of each band decreases as r increases. As, for a uniform particle distribution measured within a finite time of observation, the frequency of faster particles is higher than that of slower particles, eqn (8) embodies the necessary correction, by dividing n_k by the velocity of the band k.

We measure $f_k(L_z)$ for distances L_z from the inlet varying from 2.5 cm to 5.0 cm. The index k ranges from 1 to 3 since, even for $L_z = 2.5$ cm, we do not observe particles flowing between the external band ($k = 3$) and the cylinder wall. At each distance from the channel inlet we take a minimum of 5 different movies each of 1 s. Since in each movie we find about 15–20 particles, our statistic at each distance from the inlet is based over about 100 particles.

The observed distributions are now compared to simulation results generated with a Giesekus fluid with $\alpha = 0$, to mimic the shear rheology of the suspending PVP solution. The relaxation time is chosen as $\lambda = 2.3 \times 10^{-3}$ s, as reported in section 4.1 and in Yang *et al.*,[10] and the blockage ratio is set to $\beta = 0.08$ as in the experiments.

The calculated distributions are obtained by repeatedly running single particle simulations (in view of the low particle-loading in the experiments), and assuming radial uniformity of the particle initial positions. More specifically, we use the following procedure: 1) we find the two trajectories passing through the internal and external boundaries of a band k (for $k = 1$ we only need the external boundary); 2) we determine the initial radial positions $r_{k,in}$ and $r_{k,out}$ of such trajectories; 3) the normalized fraction $f_k(L_z)$ is calculated as: $f_k(L_z) = (r^2_{k,out} - r^2_{k,in})/R^2$. Of course, for $k = 1$, $r_{1,in} = 0$.

Fig. 5 shows the comparison of the calculated (bars) and the experimentally measured (symbols) distribution function of particles at different axial positions along the pipe. A progressive crowding around the pipe centerline is apparent, and a complete 3D focusing is eventually achieved within a few centimeters.

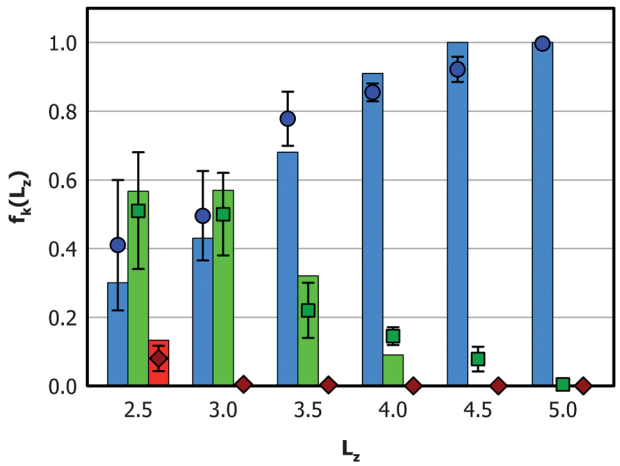

Fig. 5 Comparison of measured and predicted radial distribution f_k at various axial positions L_z. At each axial position the bars are the calculated particle fraction within $r < 2a$ (cyan), $2a < r < 4a$ (green), and $4a < r < 6a$ (red); symbols are the corresponding measured fractions.

Good quantitative agreement is found between predictions and experiments.

We observe that larger pressure drops ($\Delta p > 2$) promote focusing, *i.e.*, alignment is obtained at smaller axial distances from the inlet section. We remark that no particle is detected near to the channel wall, in agreement with the simulation results, because of the virtual absence of shear-thinning of the suspending fluid.

According to the simulation results, wall attraction becomes effective when shear-thinning of the suspending liquid is substantial. We tested such a prediction by using the robustly shear-thinning water solution of PEO. Experimental results with PEO solution do confirm the numerical simulations, as shown in Fig. 6, where the coexistence of particles flowing at the pipe centerline and particles flowing at the wall is observed, thus demonstrating the bistability scenario.

5 Design criteria for 3D-focusing in micropipes

We have just demonstrated the possibility of obtaining the focusing on a single line in a pressure-driven straight microfluidic cylindrical channel by exploiting the viscoelasticity of the suspending medium. We remark again that the focusing mechanism under consideration is a purely elastic effect.

It is worth mentioning that this kind of focusing mechanism is found to be effective over a wide range of flow rates: for the channel length used in the experiments flow focusing is observed over an interval of flow rates spanning more than one order of magnitude. Thus, the viscoelastic flow-focuser is extremely flexible. Some care, however, must be taken in choosing the suspending liquid, as the rheological properties may drive the particles towards the channel wall for the bistability behavior discussed above. In this sense, the flow focuser must be accurately rheo-engineered.

Fig. 6 Experimental particle distribution in a straight cylindrical microchannel at 8 cm from the inlet for 1% water solution of PEO. The applied pressure drop is $\Delta p = 0.2$ bar, corresponding to a flow rate $Q = 4.4 \times 10^{-3}$ μl min^{-1} and a Deborah number $De \cong 0.03$. A bistability scenario is apparent, with some particles flowing at the wall.

In order to properly design a viscoelasticity-based flow-focuser, we develop a simple heuristic argument, which is able to describe the essential features of the viscoelasticity induced cross-flow migration in micro-pipes. We consider the local flow field around the particle in terms of local shearings, namely, an upper and a lower (*i.e.*, along the radius) shear rate that have to account for the actual particle translational velocity in the main flow direction. In view of the non-Newtonian nature of the liquid, an elastic transverse force on the particle results from such local shear rates. Indeed, different shear rates around the particle give different local radial components τ_{rr} of the stress. Such stress components give forces of the order $\tau_{rr}a^2$, hence a net transverse force to be balanced (in inertia-less situations) by a drag force $F_D \cong -6\pi\eta_0 a V_M$, with V_M the cross-flow migration velocity.

The translational horizontal velocity of the particle $V_T(r)$ is needed to estimate how the local shear rate $\dot{\gamma}$ differs, in confined flows, from the velocity $v(r)$ of the unperturbed liquid at the same height in the channel.[25] Indeed, the particle can either lead or lag the flow, *i.e.*, $V_T(r) = v(r) + V_s(r)$ with $V_s(r)$ (positive or negative, respectively) the so-called slip velocity. By considering that, in the limit of small De values, the normal stress is given as $\tau_{rr} = (\Psi_1 + 2\Psi_2)\dot{\gamma}^2$,[26] the above mentioned force balance gives:

$$V_M(r) \propto -\frac{\Psi_1 + 2\Psi_2}{\eta_0}\,\frac{a^2Q^2}{R^8}\,r\left[1+\frac{R^4\,V_S(r)}{a^2Q}\right] \qquad (9)$$

where, coherently with the low De assumption, we used the Newtonian result $\dot{\gamma}(r) \cong -Q/R^4 r$. Eqn (9) predicts viscoelasticity-induced migration for a pressure-driven flow. The slip velocity in eqn (9) must be evaluated in the Newtonian limit. It was shown by Higdon and Muldowney[24] that it is always negative, and grows in absolute value with increasing r, *i.e.*, the particle always lags the fluid. Around the centerline, the term in square brackets turns out to be positive, hence, the migration velocity is negative there, *i.e.*, towards $r = 0$. On the other hand, a radial position $r = r^*$ exists, beyond which the migration velocity is towards the pipe wall. The neutral surface corresponds to $V_M(r^*) = 0$. It should be remarked that, if the effective shear rate is evaluated by neglecting the particle disturbance to the flow field (*i.e.*, by neglecting the slip velocity), the bistability is not captured.

Even though eqn (9) has been deduced by a simple heuristic argument, it correctly reproduces the simulation results. To illustrate this point, let us consider its predictions close to the pipe centerline, *i.e.*, where the square brackets is unity. Indeed, within this limit eqn (9) reads:

$$\frac{V_M(r)}{\frac{Q}{R^2}} \propto -De\left(1+2\,\frac{\Psi_2}{\Psi_1}\right)\beta^2\,\frac{r}{R} \qquad (10)$$

with ψ_1/η in eqn (9) giving the liquid relaxation time λ entering De. The linearity in De directly comes from the perturbative nature of the heuristic argument. On the other hand, the

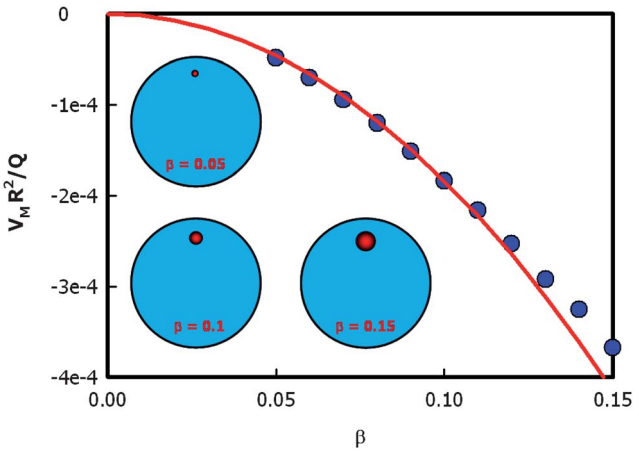

Fig. 7 Dimensionless particle migration velocity as a function of the blockage ratio computed by numerical simulations (symbols) at $r/R = 0.1$. The solid line is the best-fit curve $-m\beta^2$ with m obtained by considering the data up to $\beta = 0.11$. Deviations from the quadratic trend are observed for higher β-values. To give an idea of the range of β-values investigated, the relative dimensions of the particle and the channel are shown for three different values of the blockage ratio.

predicted dependence on the blockage ratio is verified in Fig. 7 where the migration velocity simulation data at $r/R = 0.1$ are successfully fitted with a parabolic law up to at least $\beta = 0.12$.

We are now in the position of deriving a simple tool for designing the flow-focusing micro-pipe. Let us define an alignment length L_A as the distance from the channel inlet needed to focus particles within a region of radius r_A around the centerline. This latter quantity is in fact a measure of the aligning efficiency. A design equation must then give L_A once a desired efficiency is prescribed with a given r_A value. Of course, the relationship between L_A and r_A will depend on the fluid and geometrical parameters.

The two non-zero components of the particle equation of motion are:

$$\frac{dz}{dt} = V_T(r) \tag{11}$$

$$\frac{dr}{dt} = V_M(r) \tag{12}$$

For the sake of simplicity, the horizontal velocity $V_T(r)$ in eqn (11) is approximated by its average value $Q/(\pi R^2)$. For the migration velocity $V_M(r)$ we take the expression given by eqn (10), assuming that the second normal stresses are negligible. After integrating eqn (12) over the accessible channel cross section, and with some straightforward manipulation, we end up with:

$$\frac{L_A}{R} = -\frac{A \log\left(\frac{r_A}{R-a}\right)}{\beta^2\, De} \tag{13}$$

where A is a constant.

Eqn (13) is the required design equation. We note that eqn (13) correctly predicts the asymptotic behaviors: i) for $De = 0$, *i.e.* for a Newtonian fluid, L_A is infinite, *i.e.* no alignment is possible (in the inertialess case); ii) for $\beta \to 0$, $L_A \to \infty$, since the gradient of normal stresses around the particle reduces as the particle size is smaller. Notice further that the logarithmic dependence in eqn (13) stems from the linearity in r of eqn (10).

In view of the quantitative agreement between simulations and experiments, we rely on the numerical tool to validate the heuristic eqn (13), and to evaluate the constant A. In Fig. 8a–b, the simulation results for L_A/R are used to verify the De^{-1} and $\log(r_A)$ scalings predicted from eqn (13), the validity of the β^2 scaling was in fact demonstrated in Fig. 7.

So it appears that both scalings are fully obeyed by simulation data, and thus eqn (13) can be safely applied for designing purposes. Then, the value of the parameter A is readily estimated to be 0.34. It seems worth mentioning that for $r_A/(R-a) = 0.17$, corresponding to the blue symbols/bars in Fig. 5, the alignment length is $L_A = 4.1$ cm. For $L_A/(R-a) = 0.35$, corresponding to the sum of the blue and green symbols/bars in Fig. 5, we estimate $L_A = 2.6$ cm. Both numbers are in very good agreement with the

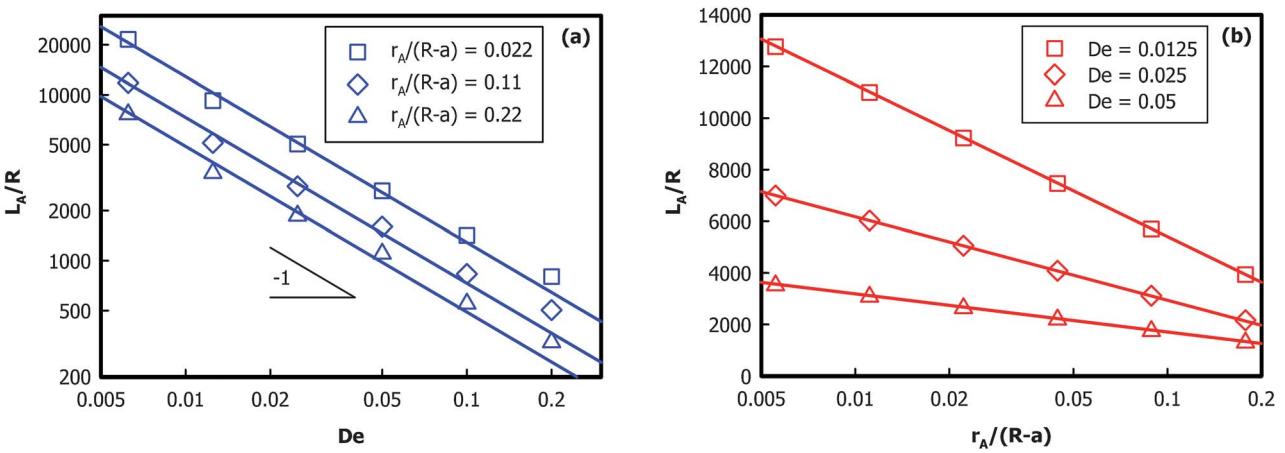

Fig. 8 (a) Dimensionless critical length as a function of the Deborah number for three values of the dimensionless critical radius. The solid curves are fits of the simulation data (symbols) through an hyperbola. The fit procedure is performed by using the data up to $De = 0.1$. For higher De values deviations are observed. (b) Dimensionless critical length as a function of the dimensionless critical radius for three values of the Deborah number. The solid curves are fits of the simulation data (symbols) through a logarithmic function.

Box 1. Design rules for viscoelastic focusing

Provided that the following assumptions hold:

- Dilute suspension ($\phi < 0.1\%$–0.2%)
- Negligible inertia ($Re < 0.1$)
- Weak shear-thinning fluid
- Relatively small blockage ratio ($\beta \leq 0.15$)

the **channel length** L_A required to focus particles within a circular cross-section of radius r_A around the channel centerline is:

$$L_A = -\frac{2\,\pi\,A\,\log\left(\frac{r_A}{R-a}\right)\,R^6}{a^2\,\lambda\,Q}$$

with $A \cong 0.34$.

In terms of pressure drop Δp, the previous equation reads as:

$$L_A = -\frac{16\,\eta_0\,L_{\mathrm{tot}}\,A\,\log\left(\frac{r_A}{R-a}\right)\,R^2}{a^2\lambda\Delta p}$$

where η_0 is the zero-shear viscosity and L_{tot} is the total channel length.

experimental results. Designing recipes stemming from eqn (13) together with the assumptions required for its validity are summarized in Box 1.

6 Conclusions

We have shown that 3D focusing of particles (*i.e.*, focusing on a line) in simple pipe flow can be attained by exploiting viscoelastic forces in flowing suspending liquids. Full 3D fluid dynamic simulations demonstrate that focusing can be finely tuned with proper rheo-engineerization of both the flow cell and the properties of the suspending liquid. Typical time and spatial scales for transversal migration make focusing attainable in microfluidic applications. Experimental results confirm viscoelasticity-induced migration of particles. Quantitative agreement between predictions and experiments is found. Simulation results support scalings deduced by a heuristic argument. Simple design criteria are then proposed to realize actual applications.

Contrarily to focusing techniques based on inertial (or inertio-elastic) effects, the viscoelastic focusing is found to work at both low and high flow rates. The lower limit is dictated by the available length of the channel whereas a reduction of the focusing efficiency at high flow rates may be induced by the arising of inertial effects. However, our experimental data shows that, in a few centimeters of channel length, one can tune the flow rate over two order of magnitude, making the viscoelastic focusing extremely flexible.

Part of our future work will be the extension of the design formula to strong shear-thinning fluids. The effect of inertia on the focusing efficiency will be also investigated.

References

1 M. Toner and D. Irimia, *Annu. Rev. Biomed. Eng.*, 2005, **7**, 77–103.
2 G. Whitesides, *Nature*, 2006, **442**, 368–373.
3 N. Pamme, *Lab Chip*, 2007, **7**, 1644–1659.
4 D. Di Carlo, *Lab Chip*, 2009, **9**, 3038–3046.
5 D. R. Gosset and D. Di Carlo, *Anal. Chem.*, 2009, **81**, 8459–8465.
6 A. A. S. Bhagat, S. S. Kuntaegowdanahalli, N. Kaval, C. J. Seliskar and I. Papautsky, *Biomed. Microdevices*, 2010, **12**, 187–195.
7 T. M. Squires and S. R. Quake, *Rev. Mod. Phys.*, 2005, **77**, 977–1026.
8 A. M. Leshansky, A. Bransky, N. Korin and U. Dinnar, *Phys. Rev. Lett.*, 2007, **98**, 234501.
9 X. Mao, S. C. S. Lin, C. Dong and T. J. Huang, *Lab Chip*, 2009, **9**, 1583–1589.
10 S. Yang, J. Y. Kim, S. J. Lee, S. S. Lee and J. M. Kim, *Lab Chip*, 2011, **11**, 266–273.
11 J. Nam, H. Lim, D. Kim, H. Jung and S. Shin, *Lab Chip*, 2012, **12**, 1347.
12 R. G. Larson, *Constitutive equations for polymer melts and solutions*, Butterworth-Heinemann, 1988.
13 G. Astarita and G. Marrucci, *Principles of Non-Newtonian Fluid Mechanics*, McGraw-Hill Inc. US, 1974.
14 G. D'Avino, P. L. Maffettone, F. Greco and M. A. Hulsen, *J. Non-Newtonian Fluid Mech.*, 2010, **165**, 466–474.
15 R. Guènette and M. Fortin, *J. Non-Newtonian Fluid Mech.*, 1995, **60**, 27–52.
16 A. C. B. Bogaerds, A. M. Grillet, G. W. M. Peters and F. P. T. Baaijens, *J. Non-Newtonian Fluid Mech.*, 2002, **108**, 187–208.
17 A. N. Brooks and T. J. R. Hughes, *Comput. Methods Appl. Mech. Eng.*, 1982, **32**, 199–259.
18 R. Fattal and R. Kupferman, *J. Non-Newtonian Fluid Mech.*, 2004, **123**, 281–285.
19 M. A. Hulsen, R. Fattal and R. Kupferman, *J. Non-Newtonian Fluid Mech.*, 2005, **127**, 27–39.
20 H. H. Hu, N. A. Patankar and M. Y. Zhu, *J. Comput. Phys.*, 2001, **169**, 427–462.
21 G. D'Avino, T. Tuccillo, P. L. Maffettone, F. Greco and M. A. Hulsen, *Comput. Fluids*, 2010, **39**, 709–721.
22 G. Segré and A. Silberberg, *Nature*, 1961, **189**, 209–210.
23 J. W. Kim and K. D. Suh, *Polymer*, 2000, **41**, 6181–6187.
24 J. J. L. Higdon and G. P. Muldowney, *J. Fluid Mech.*, 1995, **298**, 193–210.
25 B. P. Ho and L. G. Leal, *J. Fluid Mech.*, 1974, **65**, 365–400.
26 C. W. Macosko, *Rheology: Principles, Measurements and Applications*, Wiley-Interscience, New York, 1994.